**Original Article**

# Skeletal mineralization deficits and impaired biogenesis and function of chondrocyte-derived matrix vesicles in *Phospho1*$^{-/-}$ and *Phospho1/Pit1* double knockout mice†

Manisha C. Yadav[1*], Ph. D., Massimo Bottini[2,3*], Ph. D., Esther Cory[4], M. A., Kunal Bhattacharya[5], Ph. D., Pia Kuss[1], Ph. D., Sonoko Narisawa[1], Ph. D., Robert L. Sah[4], M.D. Sc. D., Laurent Beck[6], Ph. D., Bengt Fadeel[5], M.D., Ph. D., Colin Farquharson[7], Ph. D., and José Luis Millán[1], Ph. D.

[1]Sanford Children's Health Research Center, Sanford Burnham Prebys Medical Discovery Institute, La Jolla, CA, USA; [2]Department of Experimental Medicine and Surgery, University of Rome Tor Vergata, Rome, Italy; [3]Inflammatory and Infectious Disease Center, Sanford Burnham Prebys Medical Discovery Institute, La Jolla, CA, USA; [4]Department of Bioengineering, University of California San Diego, La Jolla, CA, USA; [5]Division of Molecular Toxicology, Institute of Environmental Medicine, Karolinska Institutet, Stockholm, Sweden; [6]INSERM U791, Centre for Osteoarticular and Dental Tissue Engineering (LIOAD), Nantes, Cedex, France; [7]The Roslin Institute, The University of Edinburgh, Easter Bush, Roslin, Midlothian, EH25 9RG, Scotland, UK.

*These authors contributed equally

Running title: MV-mediated initiation of mineralization

Grant support: Supported by grants R01 AR53102 and P01 AG007996 from the National Institute of Arthritis, Musculoskeletal and Skin Diseases (NIAMS), National Institutes of Health (NIH), USA. CF received funding from the Biotechnology and Biological Sciences Research Council (BBSRC), UK.

Corresponding author:
José Luis Millán, Ph. D., Professor
Sanford Burnham Prebys Medical Discovery Institute
10901 North Torrey Pines Road, La Jolla, CA 92037
Tel: 858-646-3130; millan@sbpdiscovery.org

Conflict of interest: All authors report no conflicts of interest.

†This article has been accepted for publication and undergone full peer review but has not been through the copyediting, typesetting, pagination and proofreading process, which may lead to differences between this version and the Version of Record. Please cite this article as doi: [10.1002/jbmr.2790]

**Additional Supporting Information may be found in the online version of this article.**

Initial Date Submitted August 13, 2015; Date Revision Submitted January 5, 2016; Date Final Disposition Set January 13, 2016

**Journal of Bone and Mineral Research**

**DOI 10.1002/jbmr.2790**

 

**ABSTRACT**

We have previously shown that ablation of either the *Phospho1* or *Alpl* gene, encoding PHOSPHO1 and tissue-nonspecific alkaline phosphatase (TNAP) respectively, lead to hyperosteoidosis but that their chondrocyte- and osteoblast-derived matrix vesicles (MVs) are able to initiate mineralization. In contrast, the double ablation of *Phospho1* and *Alpl* completely abolish initiation and progression of skeletal mineralization. We argued that MVs initiate mineralization by a dual mechanism: PHOSPHO1-mediated intravesicular generation of $P_i$ and phosphate transporter-mediated influx of $P_i$. To test this hypothesis, we generated mice with *col2a1*-driven cre-mediated ablation of *Slc20a1,* hereafter referred to as *Pit1,* alone or in combination with a *Phospho1* gene deletion. $P_it1^{col2/col2}$ mice did not show any major phenotypic abnormalities, while severe skeletal deformities were observed in the [$Phospho1^{-/-}$; $P_it1^{col2/col2}$] double knockout mice that were more pronounced than those observed in the $Phospho1^{-/-}$ mice. Histological analysis of [$Phospho1^{-/-}$; $P_it1^{col2/col2}$] bones showed growth plate abnormalities with a shorter hypertrophic chondrocyte zone and extensive hyperosteoidosis. The [$Phospho1^{-/-}$; $P_it1^{col2/col2}$] skeleton displayed significantly decreases in BV/TV%, trabecular number and bone mineral density, as well as decreased stiffness, decreased strength, and increased post-yield deflection compared to $Phospho1^{-/-}$ mice. Using atomic force microscopy we found that ~80% of [$Phospho1^{-/-}$; $P_it1^{col2/col2}$] MVs were devoid of mineral in comparison to ~50 % for the $Phospho1^{-/-}$ MVs and ~25% for the WT and $P_it1^{col2/col2}$ MVs. We also found a significant decrease in the number of MVs produced by both $Phospho1^{-/-}$ and [$Phospho1^{-/-}$; $P_it1^{col2/col2}$] chondrocytes. These data support the involvement of $P_i$T-1 in the initiation of skeletal mineralization and provide compelling evidence that PHOSPHO1 function is involved in MV biogenesis. 

## INTRODUCTION

Mineralization of cartilage and bone occurs by a series of physicochemical and biochemical processes that together facilitate the deposition of hydroxyapatite in specific areas of the extracellular matrix (ECM). Tissue-nonspecific alkaline phosphatase (TNAP) plays a crucial role in restricting the concentration of the mineralization inhibitor inorganic pyrophosphate ($PP_i$) to maintain a $P_i/PP_i$ ratio permissive for normal propagation of mineral in the extracellular matrix.[1-5] However, chondrocyte and osteoblast-derived matrix vesicles (MVs) from *Alpl*$^{-/-}$ mice are still able to initiate mineralization,[6, 7] indicating that other enzymes or mechanisms are involved in the intravesicular initiation of mineralization. We showed that PHOSPHO1, an enzyme that uses phosphocholine and phosphoethanolamine as substrates, is required for MV-mediated initiation of mineralization[8] as the lack of PHOSPHO1 (*Phospho1*$^{-/-}$ mice) leads to skeletal and dental hypomineralization[9] and decrease in the mechanical properties of bones[10] but not to elimination of intravesicular mineral formation. Importantly however, the [*Alpl*$^{-/-}$; *Phospho1*$^{-/-}$] double null mice are embryonic lethal and the E16.5 embryos show complete absence of skeletal mineralization and MVs devoid of mineral.[9, 11] We hypothesized that MV-mediated initiation of mineralization results from a dual mechanism, *i.e.* PHOSPHO1-mediated intra-vesicular production and transporter-mediated influx of $P_i$.[12] Two related type III Na/$P_i$ co-transporters, $P_i$T-1/Glvr1 and $P_i$T-2/Ram, are expressed by chondrocytes and osteoblasts, but $P_i$T-1 is the most abundant in these cell types.[13-15] To test the hypothesis that $P_i$-influx into MVs contributes to the initiation of mineralization, we generated mice with a conditional ablation of the $P_i$T-1 gene (*Slc20a1*, here referred to as *Pit1*) alone or in the *Phospho1*$^{-/-}$ background and we used atomic force microscopy (AFM) to quantify the number of MVs produced by *Phospho1*$^{-/-}$ and *Phospho1/Pit1* doubly deficient primary chondrocytes and Raman spectroscopy to assess the presence or absence of mineral in the MVs. Our data support the involvement of $P_i$T-1 function in the initiation of endochondral ossification and also points to PHOSPHO1 as an enzyme involved in MV biogenesis.

## MATERIALS AND METHODS

### Mice

Phospho1-R74X mutant mice (Phospho1$^{m1Jlm}$, here referred to as *Phospho1*$^{-/-}$) were previously described.[9] The generation and characterization of the *P$_i$t1*$^{flox/flox}$ mice (Slc20a1$^{tm1.1bek}$) was reported earlier.[16] To generate mice lacking both PHOSPHO1 and P$_i$T-1, *Phospho1*$^{-/-}$ and *P$_i$t1*$^{flox/flox}$ mice were crossed and double heterozygote mice were bred to generate [*Phospho1*$^{-/-}$; *P$_i$t1*$^{flox/flox}$] double mutant mice. These mice were then bred with *Col2a1-cre* mice to generate [*P$_i$t1*$^{flox/flox}$*; Col2a1-cre*], here named *P$_i$t1*$^{col2/col2}$ and [*Phospho1*$^{-/-}$; *P$_i$t1*$^{col2/col2}$] mice. *Phospho1*$^{-/-}$ genotypes were determined using genomic DNA, PCR and restriction digestion by BsrD1 restriction enzyme.[9] *P$_i$t1*$^{col2/col2}$ and [*Phospho1*$^{-/-}$; *P$_i$t1*$^{col2/col2}$] mice were genotyped by PCR. The primer sequences were: *Phospho1*: F 5' TCCTCCTCACCTTCGACTTC -3', R 5'- ATGCGGCGGAATAAACTGT -3', *P$_i$t1*$^{flox/flox}$: F 5' AAGGCATTTGTCAGCCCAGTC-3', R 5' ATCGATCCACTCAGTCTAGTGC-3' and *Col2a1-cre*: F 5'- GCCTGCATTACCGGTCGATGCAACGA -3' and R 5'- GTGGCAGATGGCGCGGCAACACCATT -3'. All mice were housed at the Sanford Burnham Prebys Medical Discovery Institute's vivarium following the guide standards (e.g. contact bedding, temperature and humidity control, etc.). All experiments reported in this manuscript were approved by the Institute under Animal Usage Form #13-058. Animal care technicians conducted routine husbandry procedures (e.g., cage cleaning, feeding and watering) and daily health checks to assess the animals' condition. To collect blood, mice were anesthetized with Avertin (0.017 ml/g body weight) and after confirmation of deep sleep, blood was obtained by cardiac puncture. The Institute's Animal Care & Use Program is accredited by AAALAC International and a Multiple Project Assurance A3053-1 is on file in the OLAW, DHHS.

### Histological and radiographic studies

Tissues were collected at either 1-month or 4-months of age as indicated and perfused with 4% paraformaldehyde (PFA) in phosphate buffered saline (PBS) and fixed for 7 days and decalcified in 10% formalin-0.125 M EDTA (pH 7.3) for 10 days prior to regular processing for paraffin sectioning. Deparaffinized sections were treated with 20 µg/ml Proteinase K in 50 mM Tris HCl-1mM EDTA-0.5% Triton X100 (pH 8.0) for 10 min at 37°C and 10 min at room temperature for unmasking. Immunostaining was processed by the ABC method (Vector Labs, Burlingame, CA) with slight modifications. SuperBlock in PBS (Life technologies, Waltham, MA) was used for blocking of the primary antibody, which was raised in rabbits against amino acids 251-380 of human $P_i$T-1 (Santa Cruz Biotechnology, Dallas, TX). In order to reduce non-specific staining, 30 min incubation with 2% normal goat serum-1% BSA-PBS was included prior to the secondary antibody as well as the ABC reagent.

Whole-body, long bones and spine radiographic images were taken using an MX20 Specimen Radiograph System (Faxitron X-ray Corporation, Chicago, IL). Paraffin or plastic sections were stained with Von Kossa/Van Gieson stain as before.[17, 18] Von Kossa/Van Gieson–stained slides were used for quantification of osteoid volume using the Bioquant Osteo Software (Bioquant Osteoanalysis Co., Nashville, TN).

### *$P_i$t1* gene expression

Primary chondrocytes from WT and *$P_i t1^{col2/col2}$* mice were isolated from the knee joint growth plates of 5 day-old pups by collagenase digestion, as described previously.[9] RNA was extracted using RNAeasy Pus Kit (Qiagen, Valencia, CA). The *$P_i$t1* primers and probe were designed using the mouse genome sequences available in the UCSC genome browser and the Genescript online primer/ probe design tool (https://www.genescript.com/ssi-bin/app/primer). A Primer BLAST search was also performed for the primers and probe sequences to check for any cross-reactivity for any other gene.

These primers/ probes were designed at exon/exon junctions so that they amplify only the cDNA and not the genomic DNA. *$P_i$t1* primers and probe sequences (Operon (San Diego, CA) are as follows: F-5'GGCTCAGGTGTAGTGACCCT3', R-5' CACATCTATCAAGCCGTTCC3' and FAM-TAMRA Probe-5'CGAAACTGTGGGCTCCGCC3'. Approximately 500 ng-1 µg of RNA were used for reverse transcription. For a 20 µl reaction, reverse transcription was carried out using the superscript kit (Life technologies, San Diego, CA) for 1 h at 42 °C followed by 70 °C for 5 min to inactivate the RT reagents. RNase H (New England Biolabs, Beverly, MA) treatment was given at 37 °C for 20 min. The RT product was then diluted with an equal volume of RNAse and DNAse free water. Specific RNA transcript (mRNA) for *Pit1* was quantified by real-time PCR using dual-labeled hydrolysis probes (FAM-TAMRA). Two µl of the (1:10) dilution of the cDNA was then used for qPCR. The reaction utilized 12.5 µl of platinum qPCR UDG Supermix (Life technologies, San Diego, CA) yielding 0.75 U Taq DNA polymerase, 20 mM Tris-HCl, 50 mM KCl, 3 mM $MgCl_2$, and 200 µM of deoxynucleoside triphosphate. Real time reaction was performed in 96-well plates on a Stratagene MX3000p real time machine (Stratagene, La Jolla, CA). The primer and probe combination that gave the lowest Ct and best amplification plots was used for the final analysis. The reaction was run at an initial temperature of 95 °C for 10 min and then at 95 °C for 30 sec, 55 °C for 1 min followed by 72 °C for 30 sec for 45 cycles. The optical signal was recorded at the end of every 72° C extension step. Ct values were determined by the software according to the optimization of the baseline. For computing the relative amounts of the target genes, the average Ct of the primary signal for 18S was subtracted from that of the target gene to give changes in Cts (dCt, a log2 scale). Amplification of the target gene was normalized to that of 18S RNA. The primers and probe sequences for mouse 18S were: F (CGGCTACCACATCCAAGGAA, 0.6 µM), R (GCTGGAATTACCGCGGCT, 0.6 µM), probe (TGCTGGCACCAGACTTGCCCTC, 0.2 µM).

**Biochemical assays**

Blood was collected by cardiac puncture into lithium heparin tubes and plasma was collected by centrifugation at 5000 rpm for 10min. Total alkaline phosphatase activity in plasma was measured using a previously reported method.[17] $PP_i$ levels were measured using activated charcoal and $^3H$ method as we previously reported.[9, 19]

**Micro–computed tomography (μCT) and histomorphometry**

Sixteen mice (4 per group) were euthanized at 1 month of age, the tibias and femurs dissected and fixed in 4% paraformaldehyde. Samples were imaged on a Skyscan 1076 μCT scanner (Kontich, Belgium). Samples were wrapped in tissue paper that was moistened with PBS, and scanned at 9 μm voxel size, applying an electrical potential of 50 kV and current of 200 μA, using a 0.5 mm aluminum filter. Mineral density was determined by calibration of images against 2 mm diameter hydroxyapatite (HA) rods (0.25 and 0.75 $gHA/cm^3$). Additionally, a beam hardening correction algorithm was applied prior to image reconstruction.

We used the software Dataviewer, CTAn and CTVox (Skyscan) to visualize and determine bone histomorphometric parameters. Cortical bone analysis was performed on the midshaft of the femurs and tibias. The volumes of interest were selected in reference to an identified landmark.[20] Since all animals were 1 month of age, the volumes of interest were (1) 3600-4500 μm proximal to the distal femur growth plate and (2) 3600-4500 μm distal to the tibia proximal growth plate. The cortical bone in this region was selected by automatic contouring of the periosteal tissue excluding the marrow cavity. A global threshold was used to identify cortical bone and an erosion of one pixel was performed to eliminate partial volume effects. From these regions of femoral and tibial cortical bone, the following parameters were determined: cross-sectional tissue area (T.Ar), cross-sectional cortical bone area (B.Ar), cortical bone area fraction (B.Ar/T.Ar), cross-sectional bone thickness (Cs.Th) and tissue

mineral density (TMD).

Trabecular bone analysis was performed at the distal femoral metaphysis and proximal tibial metaphysis. The regions of interest were (1) 360-2160 μm proximal to the distal femoral growth plate, and (2) 360-2160 μm distal to the proximal tibial growth plate. The trabecular region was selected by automatic contouring. An adaptive threshold (using the mean maximum and minimum pixel intensity values of the surrounding ten pixels) was used to identify trabecular bone and an erosion of one pixel was performed to eliminate partial volume effects. From these regions of femoral and tibial trabecular bone the following parameters were determined: tissue volume (TV), trabecular bone volume (BV), trabecular bone volume fraction (BV/TV), trabecular thickness (Tb.Th), trabecular separation (Tb.Sp), trabecular number (Tb.N), structure model index (SMI), trabecular pattern factor (Tb.Pf), and bone mineral density (BMD).

**3-point bending for the determination of bone stiffness and breaking strength**

An Instron 3342 materials' testing machine (Instron, Norwood, MA, USA) fitted with a 2 kN load cell was used to determine bone stiffness and breaking strength.[21] The span was fixed at 5.12 mm for femurs. The cross-head was lowered at 1 mm/min and data were recorded after every 0.2 N change in load and every 0.1 mm change in deflection. Each bone was tested to fracture. Failure and fracture points were identified from the load-extension curve as the point of maximum load and where the load rapidly decreased to zero, respectively. The maximum stiffness was defined as the maximum gradient of the rising portion of this curve, and the yield point was defined as the point at which the gradient was reduced to 95% of this value. Both values were calculated from a polynomial curve fitted to the rising region of the load-extension curve in Mathcad (Mathsoft Engineering and Education Inc., Cambridge, MA).[21]

**Atomic force microscopy (AFM)**

MVs were isolated from differentiating chondrocytes by differential centrifugation as described earlier.[9] A drop (5 μL) of each MV solution in Tris-buffered-saline was spotted on freshly cleaved mica substrates (Ted Pella, Redding, CA) and allowed to stand for 5 min. Next, 5 μL of glutaraldehyde solution (8% in $H_2O$, Sigma-Aldrich, St. Louis, MO) was dropped onto the samples. The substrates were stored inside a desiccators at room temperature for 24 h. AFM images of dried samples were recorded in air by means of an 5500 atomic force microscope (Agilent Technologies, Santa Clara, CA) equipped with an open-loop probe working in non-contact (AAC) mode. Silicon-nitride cantilevers having a nominal resonance frequency of ~190 kHz (NanosensorsTM, Neuchatel, Switzerland) were used. Tridimensional AFM images were generated by PicoView software (Agilent Technologies). AFM images were used to gather information about the morphology, height, volume and number of MVs in each sample. AFM phase images were also recorded on samples prepared without the use of glutaraldehyde.

**Raman spectroscopy**

MVs, suspended in Tris buffered saline, were drop-casted onto a glass slide and scanned by means of an alpha300 Raman spectrometer system (WITec GmbH, Ulm, Germany) with a laser of 532 nm wavelength and integration time of 1s. Scans were mostly performed in the central region of the drop because AFM imaging on samples prepared using a similar procedure showed a very high density of MVs and low concentration of salt crystals, which may produce background fluorescence and cover the signal from mineral aggregates inside the MVs, in that region. Six random spectra of 10 accumulations from the WT sample and 5 random spectra of 10 accumulations for the *Phospho1*$^{-/-}$ MV samples were collected at 60× magnification. Raman spectra were averaged for both WT and *Phospho1*$^{-/-}$ MV samples.

**Statistical analysis**

All measurements were performed at least in triplicate. Results are expressed as mean ± SEM. The data were analyzed using Student's t test. For microCT analysis, results are expressed as mean ± SD, statistical differences between experimental groups were analyzed using Kruskal-Wallis (K-W) test by SPSS Statistics, P values less than 0.05 were considered significant. For AFM, statistical differences between samples were calculated by non-parametric Mann–Whitney U analysis performed by SPSS Statistics (IBM Corporation, Armonk, NY).

## RESULTS

### Skeletal phenotype of [*Phospho1*$^{-/-}$; *Pit1*$^{col2/col2}$] mice

Immunohistochemistry demonstrated reduced $P_i$T-1 expression in the proliferative and hypertrophic chondrocyte area of the vertebral bones of 4 month-old *P$_i$t1*$^{col2/col2}$ mice compared to WT mice (Fig. 1A). There was visible residual $P_i$T-1 expression that was estimated to be 30% by qPCR (Fig. 1B). *P$_i$t1*$^{col2/col2}$ mice were otherwise comparable in size to WT mice. The [*Phospho1*$^{-/-}$; *P$_i$t1*$^{col2/col2}$] skeletons, however, showed exacerbated abnormalities compared to the *Phospho1*$^{-/-}$ mice, including multiple fractures and callus formation in the ribs, increased bowing of the long bones and increased prevalence of fractures in these bones (Fig. 2). Histology revealed narrower growth plates in the [*Phospho1*$^{-/-}$; *P$_i$t1*$^{col2/col2}$] bones (Fig. 3A). Histomorphometric analyses in 15-days-old mice confirmed the osteomalacia previously reported in 10-days-old and 1-month-old *Phospho1*$^{-/-}$ mice[9] (Fig. 3B and C) as compared to the WT mice and showed worsening of this phenotype in [*Phospho1*$^{-/-}$; *P$_i$t1*$^{col2/col2}$] mice with even complete absence of mineralization in areas of the trabecular bone (Fig. 3C). The secondary ossification centers also show increased amount of osteoid (Fig. 3D). The vertebral sections also showed the presence of widespread hyperosteoidosis in the *Phospho1*$^{-/-}$ mice, which further increased in [*Phospho1*$^{-/-}$; *P$_i$t1*$^{col2/col2}$] mice (Supplemental Figure 1). μCT analysis concurred with the radiographic and histology data showing enhanced bowing of the long bones in tibias and femurs of the [*Phospho1*$^{-/-}$; *P$_i$t1*$^{col2/col2}$] compared to *Phospho1*$^{-/-}$ mice (Fig. 4A, B). Trabecular parameters (Table 1) of the femurs of [*Phospho1*$^{-/-}$; *P$_i$t1*$^{col2/col2}$] compared to *Phospho1*$^{-/-}$ mice showed significantly decreased BV/TV% (p=0.021), decreased trabecular number (p=0.031), increased structure model index (p=0.006) and decreased bone mineral density (p=0.009). At the tibia, the [*Phospho1*$^{-/-}$; *P$_i$t1*$^{col2/col2}$] mice showed a significant decrease in bone mineral density (p=0.023) compared to *Phospho1*$^{-/-}$ mice. Also, the cortical parameters (Table 2) of femurs in the [*Phospho1*$^{-/-}$; *P$_i$t1*$^{col2/col2}$] compared to *Phospho1*$^{-/-}$ mice show significantly decreased relative bone area (p=0.017) and cross-sectional thickness (p=0.021), and in [*Phospho1*$^{-/-}$; *P$_i$t1*$^{col2/col2}$] compared to *P$_i$t1*$^{col2/col2}$ mice, there was

a significant decrease in relative bone area (p=0.045) cross-sectional thickness (p=0.045) and tissue mineral density (p=0.012). The cortical parameters of tibias in these mice show significant decreases in tissue mineral density (p=0.038) in [*Phospho1*$^{-/-}$; *P*$_i$*t1*$^{col2/col2}$] compared to *P*$_i$*t1*$^{col2/col2}$ mice. Three-point bending analysis showed that *P*$_i$*t1*$^{col2/col2}$ femurs break like WT, but that [*Phospho1*$^{-/-}$; *P*$_i$*t1*$^{col2/col2}$] bones take even longer deflection than *Phospho1*$^{-/-}$ bones and do not break (Supplemental Figure 2). Reduced total plasma alkaline phosphatase activity was observed in 1-month-old [*Phospho1*$^{-/-}$; *P*$_i$*t1*$^{col2/col2}$] mice compared to WT mice (p=0.012) (Supplemental Figure 3A). Consistent with the measured alkaline phosphatase levels we found increased plasma $PP_i$ levels in [*Phospho1*$^{-/-}$; *P*$_i$*t1*$^{col2/col2}$] compared to WT (p=0.012) and *Phospho1*$^{-/-}$ (p=0.04) mice (Supplemental Figure 3B).

**Analyses of MVs**

Isolated MVs imaged by atomic force microscopy (AFM), appeared as flattened globular features either individually dispersed or connected to form several micron-long chains (Supplemental Figure 4A). First, we calculated the number of MVs by counting the globular features in N=20 scan fields with an area of 1 $\mu m^2$ for each sample. The number of MVs was different among samples with the order WT = *P*$_i$*t1*$^{col2/col2}$ > *Phospho1*$^{-/-}$ ≥ [*Phospho1*$^{-/-}$; *P*$_i$*t1*$^{col2/col2}$] (Fig. 5A). Next, we modeled MVs as oblate spheroids and calculated their heights (*i.e.* the polar diameters, 2×a in Supplemental Figure 4B) by recording the cross sections of the globular features in the AFM images and measuring the values of the cross sections' peaks. The distribution of heights was different among samples. Both WT and *P*$_i$*t1*$^{col2/col2}$ MVs showed broad height distributions centered at ~7 nm, whereas *Phospho1*$^{-/-}$ and [*Phospho1*$^{-/-}$; *P*$_i$*t1*$^{col2/col2}$] MVs showed narrow distributions centered at 4.8 nm and 3.8 nm, respectively (Fig. 6A). We also calculated MV volume by calculating the equatorial diameter as the cross sections' width at half height (2×b in Supplemental Figure 4B). WT and *P*$_i$*t1*$^{col2/col2}$ MVs showed broad and right-skewed volume distributions centered at ~$140\times10^3$ $nm^3$, whereas *Phospho1*$^{-/-}$ and [*Phospho1*$^{-/-}$; *P*$_i$*t1*$^{col2/col2}$] MVs showed narrow distributions centered at $37\times10^3$ $nm^3$ and $16\times10^3$ $nm^3$, respectively

(Fig. 6B). We also found that MVs with heights smaller than ~5 nm showed a smooth surface, whereas bigger vesicles showed a non-uniform surface with irregularities that were few to several angstroms tall (Fig. 6C and 6D, respectively). Surface irregularities were interpreted as caused by the presence of mineral aggregates underneath the vesicles' membranes. These observations suggested dividing the MVs in two groups, mineral aggregate-devoid and mineral aggregate-filled MVs. In order to simplify the subsequent calculations, we considered a height threshold of ~5 nm to distinguish between the two groups of MVs for all samples. We found that the percent of aggregate-filled MVs was different among samples with the order WT = $P_it1^{col2/col2} \geq Phospho1^{-/-} > [Phospho1^{-/-}; P_it1^{col2/col2}]$(Fig. 5B).

Next, we used AFM phase analysis to gather qualitative information about the internal composition of MVs.[22, 23] These studies were performed on WT and *Phospho1*$^{-/-}$ MV samples prepared without the use of glutaraldehyde, in order to avoid the contribution on phase variations as a result of the interaction of the tip with the polymeric shell. MVs with heights smaller than ~5 nm exhibited phase angle (φ) values that were almost constant and similar to those of the mica substrate (Fig. 6E and Supplemental Figure 5A). In contrast, AFM phase images for MVs with heights greater than ~5 nm showed a great heterogeneity of φ values with bright spots that had φ values similar to those of the mica substrate surrounded by regions with negative φ values (Fig. 6F and Supplemental Figure 5B). These spots corresponded to height irregularities in topographic images. The bright spots in MV phase images were interpreted as caused by the presence of highly viscoelastic aggregates of minerals, protein, lipids and other biomolecules – *i.e.* the nucleational core (NC)[24, 25] – under the MV membrane. These aggregates were surrounded by less crowded regions which made the membrane cover deformable thus leading to negative values of φ due to viscous damping of tip vibration. The constant values of φ in phase images for MVs with heights smaller than ~5 nm suggested the absence of the NC within these MVs.

Finally, we recorded the Raman spectra for WT and *Phospho1*$^{-/-}$ MV samples to further validate the differences between the material inside MVs with different sizes and surface morphologies. Raman spectra of WT MVs showed several distinguishable peaks, which are characteristic of both the inorganic and organic matrix phases (red spectrum curve in Supplemental Figure 5). The broad peak at ~1070 $cm^{-1}$ was attributed to carbonate inorganic phase. Peaks at ~1245 $cm^{-1}$ and ~1460 $cm^{-1}$ were attributed to protein amide III and $CH_2$ deformation, respectively, whereas peaks at ~890 $cm^{-1}$, ~1297 $cm^{-1}$ and ~1437 $cm^{-1}$ (shoulder) were assigned to CH, $CH_2$ and $CH_3$, respectively, deformation modes of lipid acyl side chains.[26,27] Finally, the sets of bands at ~1120 $cm^{-1}$ were attributed to the P-O-C stretching modes of the phospholipid ester bond.[26] In contrast, Raman spectra of *Phospho1*$^{-/-}$ MVs showed very weak peaks (blue spectrum curve in Supplemental Figure 6).

**DISCUSSION**

The double ablation of PHOSPHO1 and TNAP function lead to embryos completely devoid of skeletal mineralization.[9] This double genetic experiment indicated that initiation of MV-mediated mineralization is dependent not only on intravesicular generation of $P_i$ by PHOSPHO1 but also on $P_i$ generated extravesicularly by TNAP.[9, 12] This conclusion was counterintuitive as we had largely assumed that the mM concentrations of $P_i$ present in all biological fluids would be sufficient to support initiation of mineralization. Instead, this double genetic experiment suggested that TNAP was not only required for the hydrolysis of $PP_i$ to allow for propagation of HA deposition in the extracellular matrix, but also for the perivesicular generation of $P_i$ from μM concentrations of ATP, $PP_i$ or both needed to initiate mineralization inside the MVs.[2 , 28-33] This premise implied the participation of $P_i$-transporters to incorporate the $P_i$ generated perivesicularly by TNAP.[9, 12] Type III $P_i$ transport systems, namely $P_i$T-1/ Glvr1 (*SLC20a1)* and $P_i$T-2/ Ram, are involved in $P_i$ handling by mineralizing cells (*i.e.* chondrocytes and osteoblasts)[34, 35] with $P_i$T-1 being predominantly expressed in these cells.[13-15, 35, 36] In the present study we set out to test the hypothesis that ablating $P_i$T-1 function in the context of a PHOSPHO1 deficiency would prevent skeletal mineralization to an extent analogous to what we had

observed in the *Phospho1/Alpl* double genetic experiment. A previous report[16] examining an allelic series of *$P_i$t1* mutations in mice expressing from 0% to 100% of $P_i$T-1 showed that a complete knockout of *Pit1* (0% expression) lead to a lethal phenotype at E12.5, embryos with 6% residual *$P_i$t1* expression were able to live until E15.5, and 15% *$P_i$t1* expression level was sufficient to bypass the embryonic lethality resulting instead in significant perinatal lethality.[37] Here, we resorted to a conditional ablation strategy aimed at affecting $P_i$T-1 expression in chondrocytes. Our immunohistochemical staining and qPCR data indicate that Cre-mediated ablation of *$P_i$t1*, driven by the *Col2* promoter, led not to the complete ablation of $P_i$T-1 expression in chondrocytes but to a 70% reduction. The skeleton of the *Pit1$^{col2/col2}$* animals only showed mild defects in agreement with earlier observations[37] but the [*Phospho1$^{-/-}$; Pit1$^{col2/col2}$*] double deficiency led to a compounding of the mineralization deficits caused by ablation of *Phospho1* function. However, the resulting compounded phenotype, while more severe than the *Phospho1$^{-/-}$* phenotype alone, did not approach in severity the dramatic absence of skeletal mineralization observed in the global [*Alpl$^{-/-}$; Phospho1$^{-/-}$*] double deficiency. We attribute this milder phenotype to the fact that expression of $P_i$T-1 was only reduced by 70% in our conditional ablation strategy. However, the possibility that other $P_i$ transporters (e.g. $P_i$T-2 or other yet unknown transporters) may be compensating for the downregulation of $P_i$T-1 or acting as alternative pathways cannot be ruled out. Nevertheless, the fact that ~80% of [*Phospho1$^{-/-}$*; *$P_i$t1$^{col2/col2}$*] MVs were devoid of mineral in comparison to ~50 % for the *Phospho1$^{-/-}$* MVs and ~25% for the WT and *$P_i$t1$^{col2/col2}$* MVs provides compelling proof that $P_i$T-1 acts in synergy with PHOSPHO1 during MV-mediated initiation of mineralization in chondrocytes. Figure 7 shows a schematic representation of our current understanding of the mechanisms of initiation of skeletal mineralization[12], integrating the functional roles of PHOSPHO1[8-10], NPP1[3-5, 31], TNAP[30-33], $P_i$T-1[16, 34-37] (and data presented in this paper) and osteopontin[38-41].

To enable the quantification of the number of MVs and to discern empty versus filled MVs, we used

atomic force microscopy (AFM), a method that has been extensively used to characterize natural (*e.g.* exosomes)[42, 43], synthetic lipid vesicles (*e.g.* liposomes),[44] and bacterial capsules[45] and that we recently adapted to the study of MVs.[46] Here, we used AFM analysis to characterize the number, surface morphology and filling of isolated MVs. MVs appeared as flattened globular features (modeled as oblate spheroids) with different sizes and surface morphologies among samples. WT and $P_it1^{col2/col2}$ showed heights up to twenty nanometers and volumes ranging from tens to hundreds of cubic nanometers, whereas $Phospho1^{-/-}$ and [$Phospho1^{-/-}$; $P_it1^{col2/col2}$] showed heights and volumes smaller than 10 nm and $100x10^3$ $nm^3$, respectively. AFM topographic and phase analyses showed that MVs with heights smaller than ~5 nm had a smooth surface and phase angles that were constant across vesicle surface, whereas bigger MVs showed a non-uniform surface with several angstrom tall irregularities that corresponded to spots with phase angles equal to or slightly smaller than that of mica substrate. These spots were surrounded by regions with negative phase angles. Raman spectra of WT MVs showed peaks that corresponded to vibrational modes of carbonate inorganic phase as well as proteins and lipids of organic phase, whereas those of $Phospho1^{-/-}$ MVs showed very weak peaks. Significantly, Raman spectra of WT MVs did not show the phosphate $\upsilon_1$ vibrational band at ~950 $cm^{-1}$ of amorphous calcium phosphate. Possible explanations for this phenomenon are that the phosphate groups were present as acidic $HPO_4$, whose Raman peak at ~1010 $cm^{-1}$ was covered by the intense bands around ~1070 $cm^{-1}$, and/or were tightly bound to proteins and lipids such that the phosphate $\upsilon_1$ vibrational band was shifted to higher wavelengths or significantly reduced in intensity.[26] Taken together, AFM and Raman spectroscopy analyses are compatible with our working assumption that MVs with heights greater than ~5 nm were filled with highly viscoelastic calcium and phosphate-rich nucleational cores (NCs).[24, 25] Previous studies have found that the NCs are aggregates of particles stabilized by lipids (*e.g.* phosphatidylserine and cholesterol) and proteins (mostly Annexin V).[24, 25] Our Raman data for WT MVs are in good agreement with the presence of lipid- and protein-rich aggregates inside these vesicles. Additionally, previous studies have described single NC particles

having a lateral dimension of ~7 nm and as composed by clusters of ~1 nm-in diameter dot-like subunits of $Ca^{2+}$ and $HPO^{2-}_4/PO^{3-}_4$ ions, which is in good agreement with the lateral dimensions of the WT MVs' surface irregularities. These considerations enabled us to formulate a relationship between MV biochemical make-up, size, development stage and amount of mineral aggregates within. MVs with heights smaller than ~5 nm were either devoid of a NC or filled with an amount of aggregates that did not lead to detectable changes in phase. These vesicles were at an early stage of their development. On the other hand, MVs with heights greater than ~5 nm were loaded with a NC, as suggested by the irregularities in their topographic and phase images, thus suggesting their progression to a more advanced stage of the mineralization. Additionally, these analyses allowed us to quantify the number of empty versus filled MVs and document the decreased ability of *Phospho1*$^{-/-}$ MVs to initiate mineralization, which become significantly more impaired in [*Phospho1*$^{-/-}$*; Pit1*$^{col2/col2}$] doubly deficient MV. These experimental data provide validation for the involvement of $P_i$T-1 function in the initiation of MV-mediated mineralization.

Another major finding reported in this paper is that *Phospho1* deficiency leads to a significant decrease in MV biogenesis. Both the *Phospho1*$^{-/-}$ and [*Phospho1*$^{-/-}$*; Pit1*$^{col2/col2}$] chondrocytes produced a greatly reduced number of MVs, but because *Phospho1* deficiency is the common denominator in both of these genotypes we conclude that PHOSPHO1 function is involved in MV biogenesis. The findings described in this paper enable a mechanistic explanation for three earlier experimental observations: 1) the reduced mineralization and reduced number of MVs in the dentin of [*Phospho1*$^{-/-}$*; Alpl*$^{+/-}$] mutant mice[11]; 2) the reduced mineralization and reduced number of MVs observed in cultured pre-odontoblastic cells deficient in the *Trps1* transcription factor, where both PHOSPHO1 and TNAP are downregulated[46] and 3) the synergistic effect of the combined use of PHOSPHO1 and TNAP inhibitors in suppressing vascular smooth muscle cell calcification.[47] All those earlier observations can now be mechanistically understood as follows: the genetic[11, 46] or pharmacological[47] ablation of

PHOSPHO1 function impairs MV biogenesis while also diminishing intravesicular $P_i$-generation needed to initiate mineralization as well as causing a downregulation in TNAP expression.[9] In turn, the genetic[4, 9, 46] or pharmacological ablation of TNAP function[47, 48] leads to an increase in extracellular $PP_i$, which suppresses extracellular matrix calcification, and also a reduction in perivesicular $P_i$-generation needed for $P_i$T-1 influx (Figure 7). The finding reported in this paper that PHOSPHO1 function is involved in MV biogenesis can be exploited pharmacologically for the treatment of arterial calcification and other forms of ectopic ossification.



 

**ACKNOWLEDGEMENTS**:

We acknowledge the expert help of Diana Sandoval from the Animal Facility at the Sanford Burnham Prebys Medical Discovery Institute at La Jolla, of John Shelley of the Histology Core Facility at Sanford Burnham Prebys Medical Discovery Institute at Lake Nona and the staff of the Histopathology Core Facility in La Jolla and of Dr. Birgit D. Brandner from the Unit for Chemistry, Materials and Surfaces, SP Technical Research Institute of Sweden, Stockholm, Sweden. JLM, MB and CF designed the studies. MCY, MB, KB, PK, EC, and SN performed the experiments. MCY, MB, PK, EC, SN, RLS, BF, RLS and JLM analyzed the data. MCY, MB, SN, EC, RLS, LB, CF and JLM wrote the manuscript.

 

**REFERENCES**

1. Moss DW, Eaton RH, Smith JK, Whitby LG. Association of inorganic-pyrophosphatase activity with human alkaline-phosphatase preparations. Biochem J. 1967;102(1):53-7.

2. Majeska RJ, Wuthier RE. Studies on matrix vesicles isolated from chick epiphyseal cartilage. Association of pyrophosphatase and ATPase activities with alkaline phosphatase. Biochim Biophys Acta. 1975;391(1):51-60.

3. Johnson KA, Hessle L, Vaingankar S, et al. Osteoblast tissue-nonspecific alkaline phosphatase antagonizes and regulates PC-1. Am J Physiol Regul Integr Comp Physiol. 2000;279(4):R1365-77.

4. Hessle L, Johnson KA, Anderson HC, et al. Tissue-nonspecific alkaline phosphatase and plasma cell membrane glycoprotein-1 are central antagonistic regulators of bone mineralization. Proc Natl Acad Sci U S A. 2002;99(14):9445-9.

5. Murshed M, Harmey D, Millan JL, McKee MD, Karsenty G. Unique coexpression in osteoblasts of broadly expressed genes accounts for the spatial restriction of ECM mineralization to bone. Genes Dev. 2005;19(9):1093-104.

6. Anderson HC, Hsu HH, Morris DC, Fedde KN, Whyte MP. Matrix vesicles in osteomalacic hypophosphatasia bone contain apatite-like mineral crystals. Am J Pathol. 1997;151(6):1555-61.

7. Anderson HC, Sipe JB, Hessle L, et al. Impaired calcification around matrix vesicles of growth plate and bone in alkaline phosphatase-deficient mice. Am J Pathol. 2004;164(3):841-7.

8. Roberts S, Narisawa S, Harmey D, Millan JL, Farquharson C. Functional involvement of PHOSPHO1 in matrix vesicle-mediated skeletal mineralization. J Bone Miner Res. 2007;22(4):617-27.

9. Yadav MC, Simão AM, Narisawa S, et al. Loss of skeletal mineralization by the simultaneous ablation of PHOSPHO1 and alkaline phosphatase function: a unified model of the mechanisms of initiation of skeletal calcification. J Bone Miner Res. 2011;26(2):286-97.

 

10. Huesa C, Yadav MC, Finnila MA, et al. PHOSPHO1 is essential for mechanically competent mineralization and the avoidance of spontaneous fractures. Bone. 2011;48(5):1066-74.

11. McKee MD, Yadav MC, Foster BL, et al. Compounded PHOSPHO1/ALPL deficiencies reduce dentin mineralization. J Dent Res. 2013;92(8):721-7.

12. Millan JL. The role of phosphatases in the initiation of skeletal mineralization. Calcif Tissue Int. 2013;93(4):299-306.

13. Nielsen LB, Pedersen FS, Pedersen L. Expression of type III sodium-dependent phosphate transporters/retroviral receptors mRNAs during osteoblast differentiation. Bone. 2001;28(2):160-6.

14. Polewski MD, Johnson KA, Foster M, Millan JL, Terkeltaub R. Inorganic pyrophosphatase induces type I collagen in osteoblasts. Bone. 2010;46(1):81-90.

15. Yoshiko Y, Candeliere GA, Maeda N, Aubin JE. Osteoblast autonomous Pi regulation via Pit1 plays a role in bone mineralization. Mol Cell Biol. 2007;27(12):4465-74.

16. Beck L, Leroy C, Beck-Cormier S, et al. The phosphate transporter PiT1 (Slc20a1) revealed as a new essential gene for mouse liver development. PLoS One. 2010;5(2):e9148.

17. Millan JL, Narisawa S, Lemire I, et al. Enzyme replacement therapy for murine hypophosphatasia. J Bone Miner Res. 2008;23(6):777-87.

18. Narisawa S, Frohlander N, Millan JL. Inactivation of two mouse alkaline phosphatase genes and establishment of a model of infantile hypophosphatasia. Dev Dyn. 1997;208(3):432-46.

19. McGuire MB, Colman CH, Baghat N, Russell RG. Radiometric measurement of pyrophosphate in cell cultures. Biochem Soc Trans. 1980;8(5):529-30.

20. Bouxsein ML, Boyd SK, Christiansen BA, et al. Guidelines for assessment of bone microstructure in rodents using micro-computed tomography. J Bone Miner Res. 2010;25(7):1468-86.

21. Aspden RM. Mechanical testing of bone ex vivo. Methods Mol Med. 2003;80:369-79.

22. Scott WW, Bhushan B. Use of phase imaging in atomic force microscopy for measurement of viscoelastic contrast in polymer nanocomposites and molecularly thick lubricant films. Ultramicroscopy. 2003;97(1-4): 151-69.

23. Anczykowski B, Gottsman B, Fuchs H, Cleveland JP, Elings VB. How to measure energy dissipation in dynamic mode atomic force microscopy. Appl Surf Sci. 1999;140 (3-4): 376-382.

24. Wu LN, Genge BR, Dunkelberger DG, LeGeros RZ, Concannon B, Wuthier RE. Physicochemical characterization of the nucleational core of matrix vesicles. J Biol Chem. 1997; 272(7): 4404-11.

25. Wuthier RE, Lipscomb GF. Matrix vesicles: structure, composition, formation and function in calcification. Front Biosci (Landmark Ed). 2011;16: 2812-902.

26. Sauer GR, Zunic WB, Durig JR, Wuthier RE. Fourier transform Raman spectroscopy of synthetic and biological calcium phosphates. Calcif Tissue Int. 1994; 54(5): 414-20.

27. Shah FA, Zanghellini E, Matic A, Thomsen P, Palmquist A. The orientation of nanoscale apatite platelets in relation to osteoblastic-osteocyte lacunae on trabecular bone surface. Calcif Tissue Int. 2015. [Epub ahead of print]

28. Robison R. The possible significance of hexosephosphoric esters in ossification. By Robert Robison, 1923. Clin Orthop Relat Res. 1991(267):2-7.

29. Hsu HH, Anderson HC. Calcification of isolated matrix vesicles and reconstituted vesicles from fetal bovine cartilage. Proc Natl Acad Sci U S A. 1978;75(8):3805-8.

30. Pizauro JM, Demenis MA, Ciancaglini P, Leone FA. Kinetic characterization of a membrane-specific ATPase from rat osseous plate and its possible significance on endochodral ossification. Biochim Biophys Acta. 1998;1368(1):108-14.

31. Ciancaglini P, Simao AM, Camolezi FL, Millan JL, Pizauro JM. Contribution of matrix vesicles and alkaline phosphatase to ectopic bone formation. Braz J Med Biol Res. 2006;39(5):603-10.

 

32. Ciancaglini P, Yadav MC, Simão AM, et al. Kinetic analysis of substrate utilization by native and TNAP-, NPP1-, or PHOSPHO1-deficient matrix vesicles. J Bone Miner Res. 2010;25(4):716-23.

33. Simao AM, Yadav MC, Narisawa S, et al. Proteoliposomes harboring alkaline phosphatase and nucleotide pyrophosphatase as matrix vesicle biomimetics. J Biol Chem. 2010;285(10):7598-609.

34. Palmer G, Guicheux J, Bonjour JP, Caverzasio J. Transforming growth factor-beta stimulates inorganic phosphate transport and expression of the type III phosphate transporter Glvr-1 in chondrogenic ATDC5 cells. Endocrinology. 2000;141(6):2236-43.

35. Palmer G, Zhao J, Bonjour J, Hofstetter W, Caverzasio J. In vivo expression of transcripts encoding the Glvr-1 phosphate transporter/retrovirus receptor during bone development. Bone. 1999;24(1):1-7.

36. Suzuki A, Ghayor C, Guicheux J, et al. Enhanced expression of the inorganic phosphate transporter Pit-1 is involved in BMP-2-induced matrix mineralization in osteoblast-like cells. J Bone Miner Res. 2006;21(5):674-83.

37. Bourgine A, Pilet P, Diouani S, et al. Mice with hypomorphic expression of the sodium-phosphate cotransporter PiT1/Slc20a1 have an unexpected normal bone mineralization. PLoS One. 2013;8(6):e65979.

38. Harmey D, Johnson KA, Zelken J, et al. Elevated skeletal osteopontin levels contribute to the hypophosphatasia phenotype in *Akp2(-/-)* mice. J. Bone Miner. Res. 2006;21(9):1377-1386.

39. Narisawa S., Yadav M.C., Millan J.L. In vivo over-expression of tissue-nonspecific alkaline phosphatase increases skeletal mineralization and affects the phosphorylation status of osteopontin. J Bone Miner Res. 2013;28(7):1587-98.

40. Foster BL, Nagatomo KJ, Tso HW, et al. Tooth root dentin mineralization defects in a mouse model of hypophosphatasia. J Bone Miner Res. 2013;28(2):271-82.

41. McKee M.D., Hoac B., Addison W.N., et al. Extracellular matrix mineralization in periodontal tissues: Noncollagenous matrix proteins, enzymes, and relationship to hypophosphatasia and X-linked hypophosphatemia. Periodontol 2000. 2013;63(1):102-122.

42. Palanisamy V, Sharma S, Deshpande A, et al. Nanostructural and transcriptomic analyses of human saliva derived exosomes. PLoS One. 2010;5(1):e8577.

43. Sharma S, Rasool HI, Palanisamy V, et al. Structural-mechanical characterization of nanoparticle exosomes in human saliva, using correlative AFM, FESEM, and force spectroscopy. ACS Nano. 2010;4(4):1921-6.

44. Teschke O, de Souza EF. Liposome structure imaging by atomic force microscopy: Verification of improved liposome stability during adsorption of multiple aggregated vesicles. Langmuir. 2002;18(17):6513-20.

45. Stukalov O, Korenevsky A, Beveridge TJ, Dutcher JR. Use of atomic force microscopy and transmission electron microscopy for correlative studies of bacterial capsules. Appl Environ Microbiol. 2008; 74(17):5457-65.

46. Kuzynski M, Goss M, Bottini M, et al. Dual role of the Trps1 transcription factor in dentin mineralization. J Biol Chem. 2014;289(40):27481-93.

47. Kiffer-Moreira T, Yadav MC, Zhu D, et al. Pharmacological inhibition of PHOSPHO1 suppresses vascular smooth muscle cell calcification. J Bone Miner Res. 2013;28(1):81-91.

48. Sheen CR, Kuss P, Narisawa S, et al. Pathophysiological role of vascular smooth muscle alkaline phosphatase in medial artery calcification. J Bone Miner Res. 2015;30(5):824-36.

Table 1: Trabecular bone morphometric parameters of the femur and tibia. Kruskal-Wallis (mean±SD, n=4). Differences at $p<0.05$ are indicated by [a] vs WT, [b] vs *Phospho1-/-*, [c] vs $P_it1^{col2/col2}$

| Sample | Site | Tissue volume TV $mm^3$ | Bone Volume BV $mm^3$ | Relative Bone Volume BV/TV% | Trabecular Thickness Tb.Th mm | Trabecular Separation Tb.Sp mm | Trabecular Number Tb.N 1/mm | Structure Model Index SMI | Trabecular Pattern Factor Tb.Pf 1/mm | Bone Mineral Density BMD $g/cm^3$ |
|---|---|---|---|---|---|---|---|---|---|---|
| **WT** | Femur | 1.77 ±0.23 | 0.17 ±0.081 | 9.33 ±3.48 | 0.039 ±0.002 | 0.21 ±0.061 | 2.36 ±0.76 | 1.97 ±0.24 | 27.17 ±6.64 | 0.22 ±0.08 |
| ***Phospho1*$^{-/-}$** | Femur | 2.17 ±0.32 | 0.14 ±0.04 | 6.50 ±0.88 | 0.035 ±0.002 | 0.21 ±0.02 | 1.86 ±0.23 | 2.13 ±0.05 | 33.75 ±2.48 | 0.17 ±0.02 |
| ***Pit1*$^{col2/col2}$** | Femur | [a]2.57 ±0.28 | 0.15 ±0.03 | 5.74 ±0.92 | [a] 0.033 ±0.001 | 0.24 ±0.04 | 1.72 ±0.25 | 2.18 ±0.05 | 35.76 ±1.87 | 0.14 ±0.02 |
| **[*Phospho1*$^{-/-}$; *Pit1*$^{col2/col2}$]** | Femur | [c]1.56 ±0.44 | [a,b,c] 0.05 ±0.03 | [a,b] 3.11 ±1.35 | [a] 0.033 ±0.003 | 0.30 ±0.06 | [a,b,c] 0.93 ±0.37 | [a,b] 2.44 ±0.11 | [a,b] 43.81 ±6.90 | [a,b] 0.10 ±0.02 |
| **K-W p-values** | Femur | *0.016* | *0.048* | *0.018* | *0.029* | *0.072* | *0.023* | *0.015* | *0.009* | *0.015* |
| **WT** | Tibia | 1.10 ±0.25 | 0.05 ±0.03 | 4.57 ±1.75 | 0.029 ±0.003 | 0.23 ±0.05 | 1.53 ±0.47 | 2.18 ±0.10 | 39.37 ±5.46 | 0.17 ±0.04 |
| ***Phospho1*$^{-/-}$** | Tibia | 1.64 ±0.33 | 0.07 ±0.02 | 4.49 ±0.39 | 0.029 ±0.001 | 0.22 ±0.01 | 1.56 ±0.13 | 2.15 ±0.05 | 39.63 ±2.13 | 0.16 ±0.01 |
| ***Pit1*$^{col2/col2}$** | Tibia | [a] 1.87 ±0.39 | 0.07 ±0.02 | 3.52 ±0.62 | 0.028 ±0.001 | 0.26 ±0.03 | 1.24 ±0.20 | 2.23 ±0.09 | 41.52 ±2.83 | 0.12 ±0.01 |
| **[*Phospho1*$^{-/-}$; *Pit1*$^{col2/col2}$]** | Tibia | [b,c] 1.09 ±0.29 | 0.04 ±0.01 | 3.30 ±0.41 | 0.03 ±0.004 | 0.26 ±0.01 | 1.10 ±0.10 | [b] 2.34 ±0.10 | 43.31 ±1.8 | [a,b] 0.11 ±0.00 |
| **K-W p-values** | Tibia | *0.024* | *0.089* | *0.20* | *0.94* | *0.12* | *0.10* | *0.076* | *0.334* | *0.017* |

Table 2: Cortical bone morphometric parameters of the femur and tibia Kruskal-Wallis (mean±SD, n=4). Differences at $p<0.05$ are indicated by [a] vs WT, [b] vs *Phospho1-/-*, [c] vs *Pit1*$^{col2/col2}$

| Sample | Site | Cross-sectional Tissue Area T.Ar $mm^2$ | Cross-sectional Bone Area B.Ar $mm^2$ | Relative Bone Area B.Ar/T.Ar % | Cross-sectional Thickness Cs.Th mm | Tissue Mineral Density TMD $g/cm^3$ |
|---|---|---|---|---|---|---|
| **WT** | Femur | 1.50 ±0.19 | 0.65 ±0.18 | 42.95 ±6.74 | 0.16 ±0.03 | 0.89 ±0.03 |
| ***Phospho1*$^{-/-}$** | Femur | [a] 1.82 ±0.13 | 0.73 ±0.08 | 40.19 ±3.99 | 0.15 ±0.02 | 0.87 ±0.05 |
| ***Pit1*$^{col2/col2}$** | Femur | 1.67 ±0.07 | 0.65 ±0.07 | 38.97 ±2.89 | 0.14 ±0.01 | 0.90 ±0.01 |
| **[*Phospho1*$^{-/-}$; *Pit1*$^{col2/col2}$]** | Femur | [b] 1.53 ±0.17 | 0.48 ±0.11 | [a,b,c] 30.84 ±4.57 | [a,b,c] 0.11 ±0.02 | [a,c] 0.85 ±0.02 |
| **K-W p-values** | Femur | *0.041* | *0.079* | *0.029* | *0.027* | *0.049* |
| **WT** | Tibia | 1.50 ±0.26 | 0.64 ±0.21 | 42.04 ±7.72 | 0.16 ±0.03 | 1.01 ±0.06 |
| ***Phospho1*$^{-/-}$** | Tibia | 1.61 ±0.17 | 0.67 ±0.09 | 41.60 ±3.37 | 0.15 ±0.02 | [a] 0.92 ±0.03 |
| ***Pit1*$^{col2/col2}$** | Tibia | 1.70 ±0.11 | 0.61 ±0.07 | 35.82 ±1.82 | 0.13 ±0.01 | 0.93 ±0.01 |
| **[*Phospho1*$^{-/-}$; *Pit1*$^{col2/col2}$]** | Tibia | 1.45 ±0.22 | 0.51 ±0.12 | 34.67 ±3.61 | 0.12 ±0.01 | [a,c] 0.87 ±0.03 |
| **K-W p-values** | Tibia | *0.434* | *0.270* | *0.117* | *0.106* | *0.020* |

**LEGEND TO FIGURES**

Fig.1: Conditional ablation of *Pit1* in chondrocytes. (A) Immunohistochemistry using anti-$P_iT$-1 antibody on the vertebral bones of 4-month-old WT and $P_it1^{col2/col2}$ mice showed reduced $P_iT$-1 expression in the hypertrophic chondrocyte region of $P_it1^{col2/col2}$ mice while $P_iT$-1 expression in skeletal muscle and hematopoietic cells remained unchanged. BM: bone marrow; SM: smooth muscle. Bar=100 µm. B) qRT-PCR of RNA extracted from 5-day-old chondrocytes (n=3) revealed ~30% residual $P_it1$ gene expression compared to WT chondrocytes (n=3).

Fig. 2: Phenotypic abnormalities in the skeleton of 1-month-old [$Phospho1^{-/-}$; $P_it1^{col2/col2}$] mice. Radiographic images of representative mice showing worsening of the skeletal abnormalities (arrows) in [$Phospho1^{-/-}$; $P_it1^{col2/col2}$] mice as compared to the $Phospho1^{-/-}$ mice (n = 10). Arrows show highly bowed long bones and multiple fractures in the spine and limbs in [$Phospho1^{-/-}$; $P_it1^{col2/col2}$] mice.

Fig. 3: Histomorphometric analyses of 15-day-old tibias of $Phospho1^{-/-}$ and [$Phospho1^{-/-}$; $P_it1^{col2/col2}$] mice. Von Kossa/van Gieson staining of the tibial section at the knee joint in WT and $P_it1^{col2/col2}$ mice showed no statistically significant difference in the growth plate (A) as well as the BV/TV and OV/BV ratios in the trabecular bone (B and C) and the secondary ossification center (D). This analysis showed trabecular bone surrounded by widespread, extended osteoid in $Phospho1^{-/-}$ mice (arrows show smaller growth plate (A) and the areas where the osteoid is present). The [$Phospho1^{-/-}$; $P_it1^{col2/col2}$] mice show even smaller growth plate (A) and more unmineralized bone in tibia. A-10X, B,C and D-20X magnification (n = 3).

Fig. 4: µCT analysis of 1-month-old femurs and tibias of WT, $Phospho1^{-/-}$, $P_it1^{col2/col2}$ and [$Phospho1^{-/-}$; $P_it1^{col2/col2}$] mice. (A) 3D volume renders of the samples (anterior view-femur, anterior view-tibia, side

view–full leg, ,) (B) 2D coronal and transaxial cross-sections of femurs and tibias. Scale bar = 1 mm. Both volume renders and cross-sections show highly bowed/ twisted long bones in [*Phospho1*$^{-/-}$*; P*$_i$*t1*$^{col2/col2}$] mice compared to WT, *P*$_i$*t1*$^{col2/col2}$ and even *Phospho1*$^{-/-}$ mice.

Fig. 5: Determination of the number of MVs and percentage of filled MVs isolated from chondrocytes of each genotype. A) The *Phospho1*$^{-/-}$ MV preparations show a statistically significant decrease in the total number of produced MVs compared to those isolated from WT chondrocytes. The [*Phospho1*$^{-/-}$*; P*$_i$*t1*$^{col2/col2}$] MV preparations also showed a significant decrease in the number of MVs compared to those isolated from WT and *P*$_i$*t1*$^{col2/col2}$ chondrocytes. The difference between the number of MVs isolated from *Phospho1*$^{-/-}$ and [*Phospho1*$^{-/-}$*; P*$_i$*t1*$^{col2/col2}$] chondrocytes was borderline significant ($p$=0.056). B) We observed a statistically significant decrease in the number of filled MVs in the [*Phospho1*$^{-/-}$*; P*$_i$*t1*$^{col2/col2}$] MV samples compared to the WT, *Phospho1*$^{-/-}$ and *P*$_i$*t1*$^{col2/col2}$ MV samples.

Fig. 6: Atomic force microscopy (AFM) images were recorded in non-contact (AAC) mode. Height (A) and volume (B) distributions were calculated for MVs isolated from WT, *Phospho1*$^{-/-}$, *P*$_i$*t1*$^{col2/col2}$ and [*Phospho1*$^{-/-}$*; P*$_i$*t1*$^{col2/col2}$] mice. MV volumes were calculated by assuming MVs as spheroidal structures (see Supplemental Figure 4B). All peaks were fitted by Gaussian curves. C-F) Images of mineral aggregate-unfilled (C and E) and filled (D and F) WT (C, D and F) and *Phospho1*$^{-/-}$ (E) MVs. From left to right: topography image, amplitude image and three-dimensional reconstruction of topography image (C and D); three-dimensional reconstructions of topography and phase images (E and F). Scale bars = 100 nm.

Fig. 7: Schematic detailing our current understanding of the biochemical bases for the steps of MV-mediated initiation of skeletal mineralization. Current data are compatible with the following interpretation: MVs initiate mineral deposition by accumulation of $P_i$ generated intravesicularly by the

action of PHOSPHO1 on phosphocholine and also via $P_i$T-1-mediated incorporation of $P_i$ generated extravesicularly by TNAP or NPP1. As shown in the current paper, PHOSPHO1 function also appears to be implicated in the biogenesis of MVs. The extravesicular propagation of mineral onto the collagenous matrix is mainly controlled by the pyrophosphatase activity of TNAP that restricts the concentration of this potent mineralization inhibitor to establish a $PP_i/P_i$ ratio conducive for controlled calcification. Additionally, osteopontin (OPN), another potent mineralization inhibitor that binds to HA mineral as soon as it is exposed to the extracellular fluid, also restricts the degree of extracellular matrix mineralization. ECM: extracellular matrix; HA: hydroxyapatite OPN: osteopontin.



 

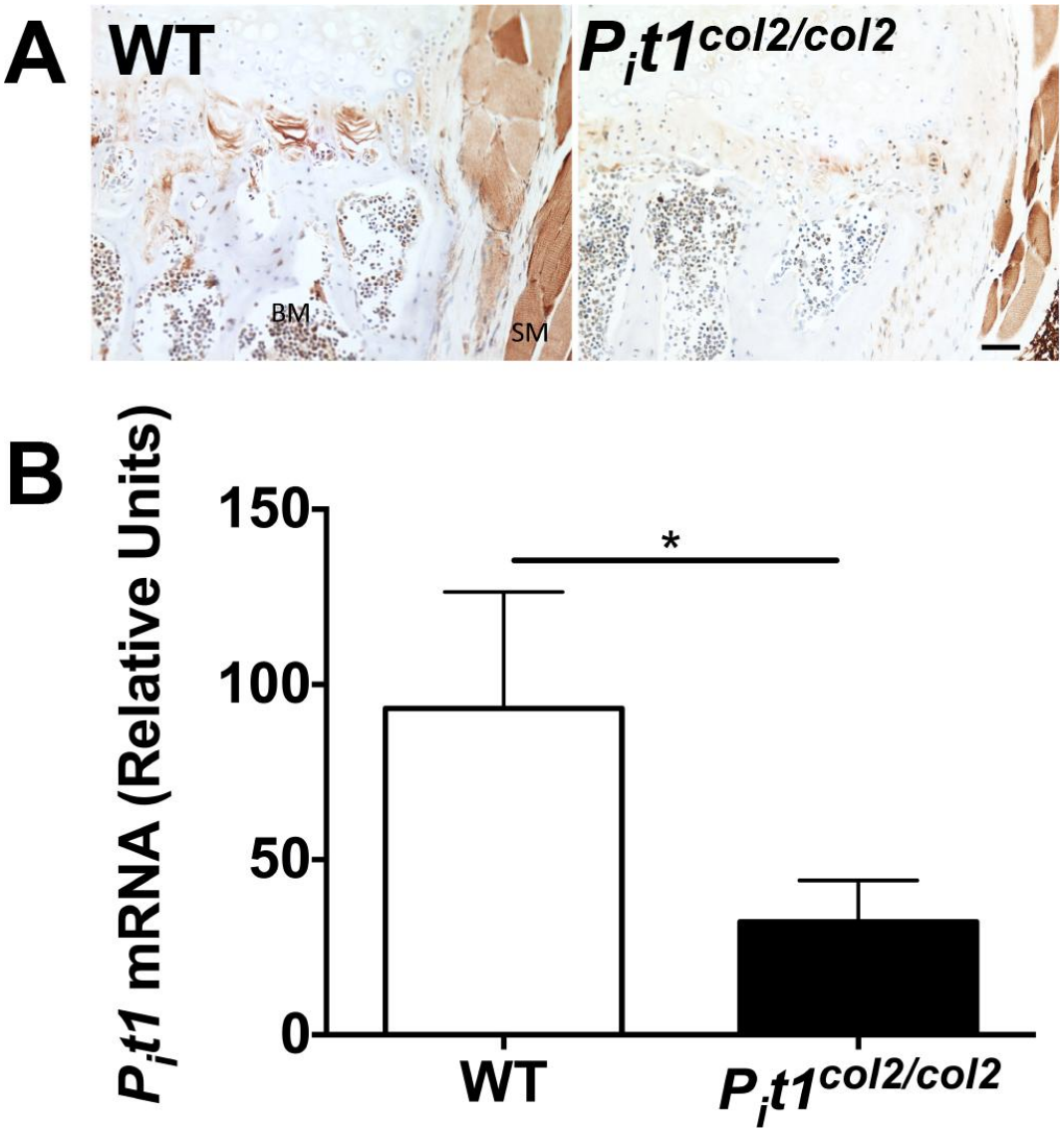


**Figure 1**

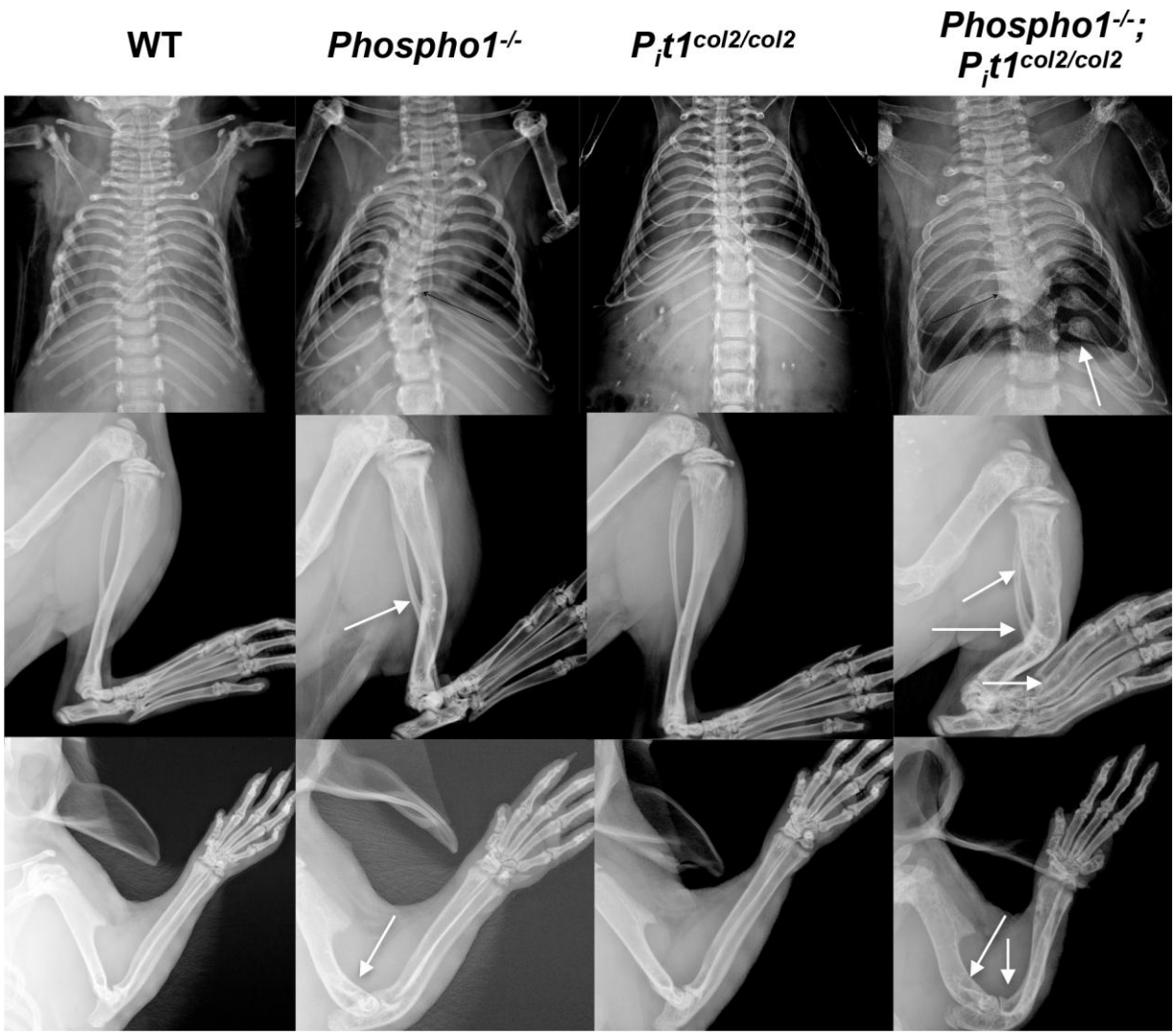


**Figure 2**

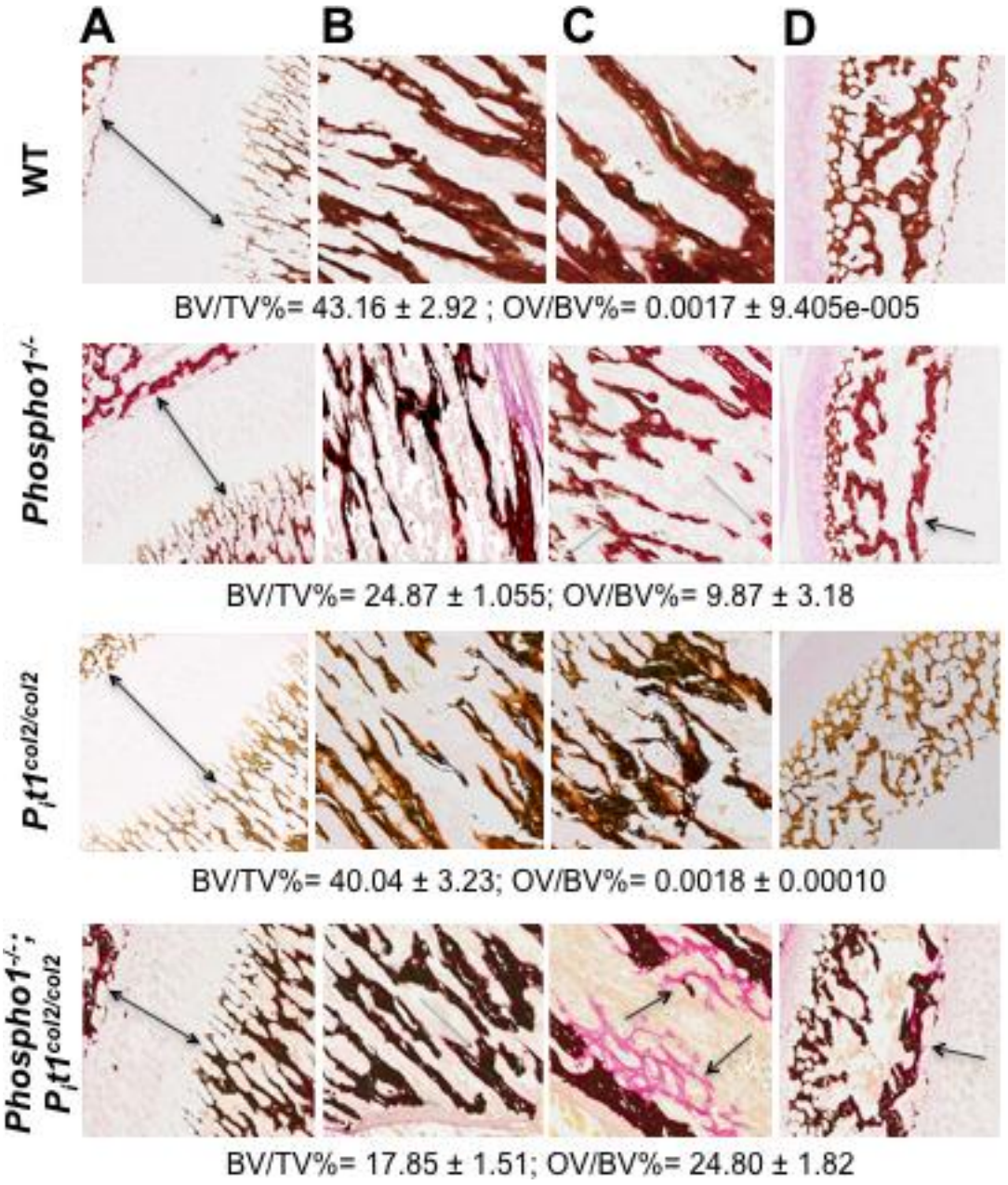


**Figure 3**

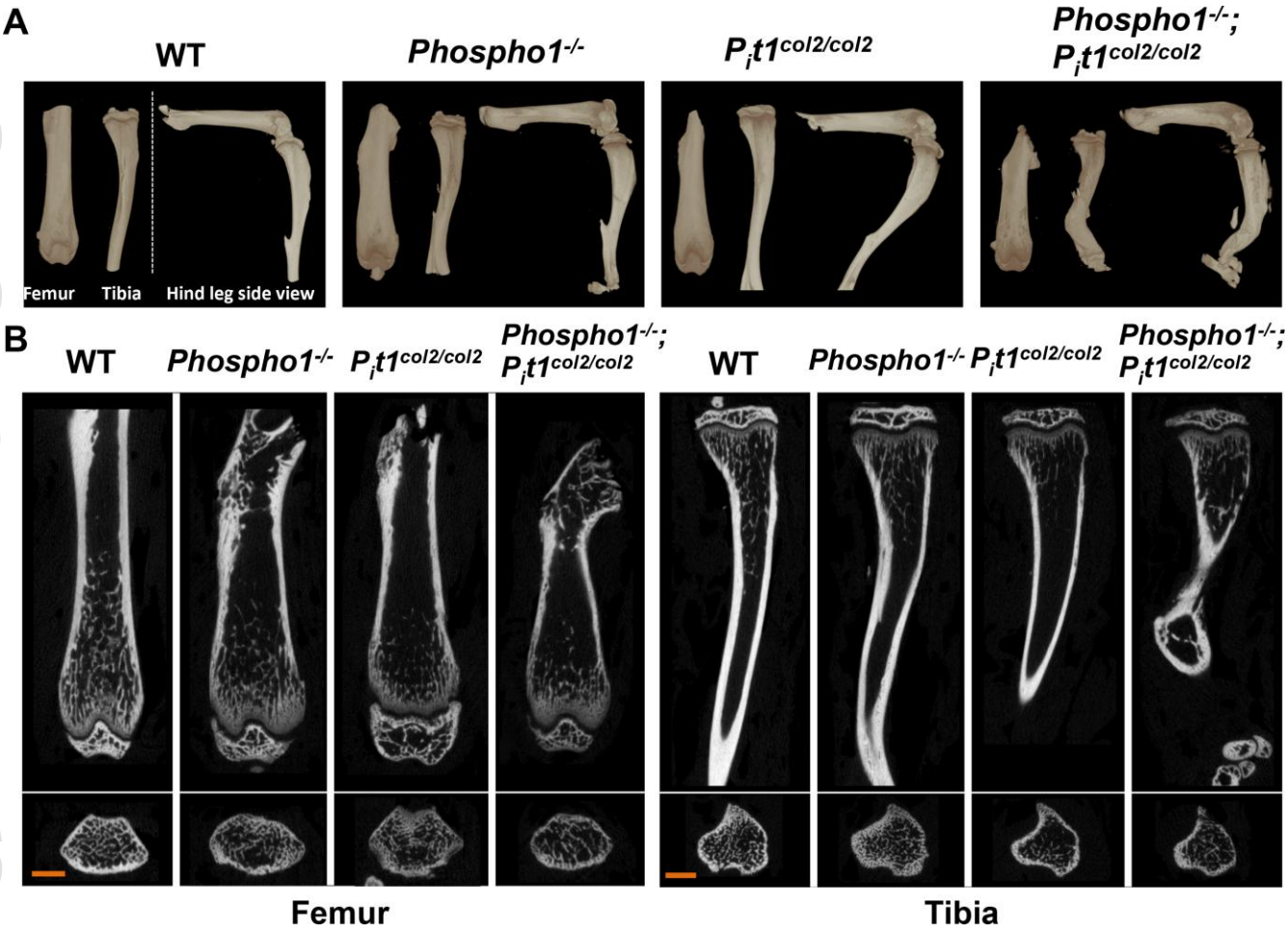


**Figure 4**

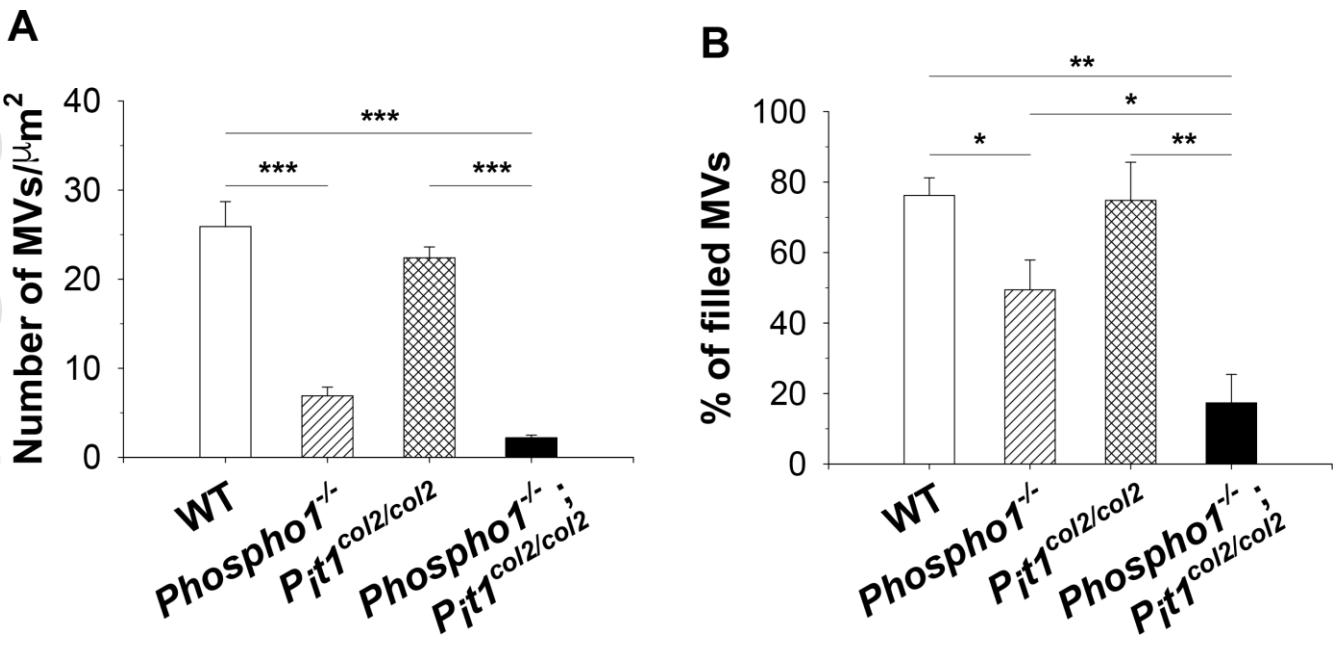


**Figure 5**

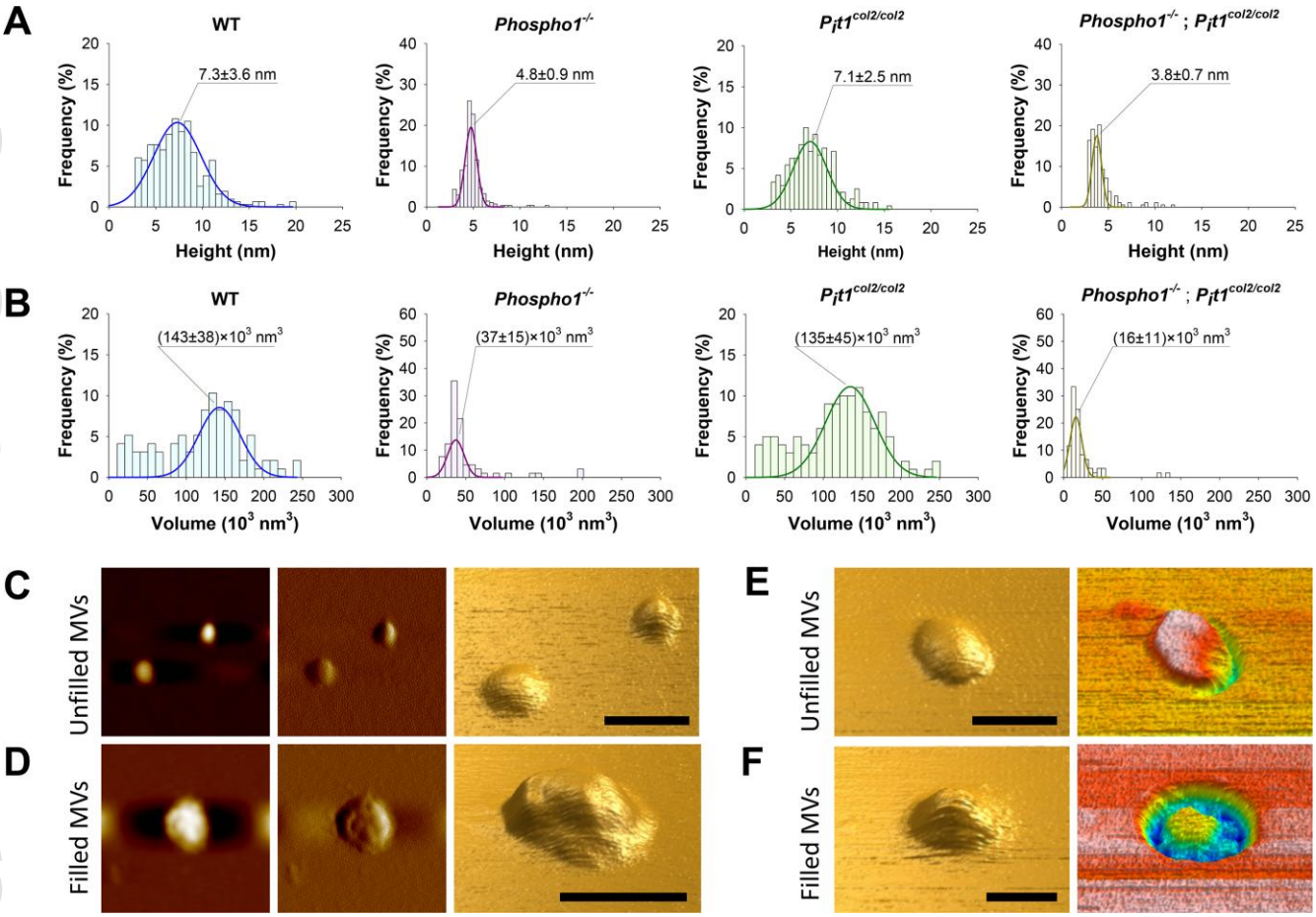


**Figure 6**

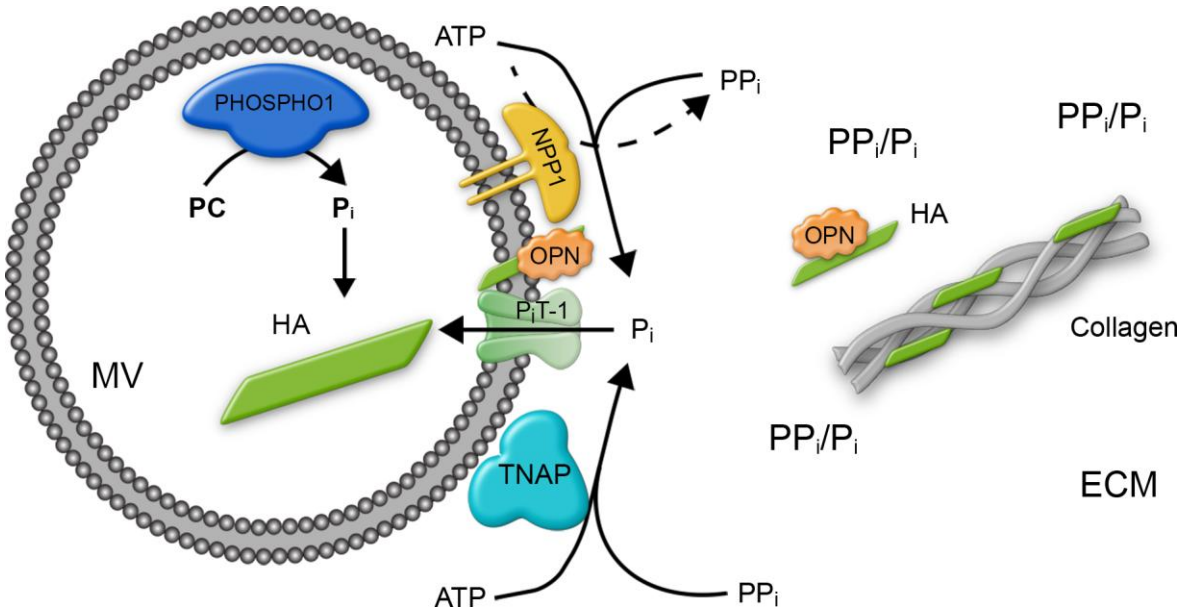


**Figure 7**